Atmos. Chem. Phys. Discuss., https://doi.org/10.5194/acp-2019-417
Manuscript under review for journal Atmos. Chem. Phys.
Discussion started: 13 May 2019

Atmospheric Chemistry and Physics Discussions

Global nighttime atomic oxygen abundances from resampled GOMOS hydroxyl airglow measurements in the mesopause region

Qiuyu Chen[1,2], Martin Kaufmann[1,2], Yajun Zhu[1], Jilin Liu[1,2], Ralf Koppmann[2], and Martin Riese[1,2]

[1]Institute for Energy and Climate Research, Forschungszentrum Jülich, Jülich, Germany
[2]Institute for Atmospheric and Environmental Research, University of Wuppertal, Wuppertal, Germany

Correspondence: Yajun Zhu (y.zhu@fz-juelich.de)

Abstract. This paper presents a new dataset of nighttime atomic oxygen density [O], derived from OH(8–4) ro-vibrational band emissions, using a non-local thermal equilibrium model, with the aim of offering new insight into the atomic oxygen abundances in the mesopause region. The dataset is based on the level-1 atmospheric background measurements observed by the GOMOS instrument on board Envisat. Raw data are reprocessed into monthly zonal mean values in 10° latitude bins with a fixed altitude grid of 3 km. The dataset spans from 70° S to 70° N in latitude and from 80 km to 100 km in altitude, covering a time period from May 2002 to December 2011 at local times of from 10 p.m. to 12 p.m..

The atomic oxygen density peaks at about 95 km and the highest values are in the range of 3–8$\times 10^{11}$ atoms cm^{-3}, depending on latitude and season. There is a rapid decrease of [O] below its peak region. The annual oscillation (AO), semiannual oscillation (SAO), and the solar cycle impact are distinguished from the [O] longtime series variations. This new GOMOS [O] dataset conforms to other published datasets and is consistent with the [O] datasets obtained from the SCIAMACHY OH airglow measurements to within about $\pm$20 %.

1 Introduction

In the middle and upper atmosphere, atomic oxygen (O) is mainly produced by molecular oxygen and ozone photolysis, and transported downward by diffusion and mixing from the thermosphere to the mesopause. Its lifetime varies from over one week at 100 km to around one day at 80 km due to its increasing chemical loss rate with decreasing altitude (Brasseur and Solomon, 2005). Atomic oxygen is one of the most abundant reactive trace species in the upper mesosphere/lower thermosphere (MLT) region and plays a crucial role in the photochemical equilibrium and energy balance of this region. Most exothermic chemical reactions, which heat the MLT region, are associated with atomic oxygen (Brasseur and Offermann, 1986; Riese et al., 1994; Mlynczak et al., 2013c). The collisions between O and infrared-active greenhouse gases like CO_2 also predominantly lead to radiative cooling in this region (Mlynczak et al., 2013a).

The measurement of atomic oxygen dates back to before the satellite era when the MLT region was explored by means of sounding rocket experiments, hosting resonance fluorescence instruments, or mass spectrometers (Dickinson et al., 1974, 1980; Sharp, 1980; Offermann et al., 1981; Sharp, 1991). They are capable of providing direct in situ measurements of atomic

Atmos. Chem. Phys. Discuss., https://doi.org/10.5194/acp-2019-417
Manuscript under review for journal Atmos. Chem. Phys.
Discussion started: 13 May 2019

Atmospheric Chemistry and Physics Discussions

oxygen, although it is difficult to obtain a consistent global picture of absolute density values from these measurements, which differ by a factor of more than 40 (Sharp, 1991).

However, these measurements lead to the development of photochemical models of the Earth's day- and nightglow, which enables the use of proxies of the atomic oxygen abundance obtained from satellite observations. Suitable proxies are airglow emissions (e.g. OH^*, O_2^*, $O(^1S)$) and thermal emissions (e.g. O_3 at 9.6 μm), in combination with corresponding photochemical models. The hydroxyl (OH) airglow emissions are associated with the spontaneous radiative transitions of excited OH^* radicals from higher to lower states. These OH^* radicals are mainly produced by the chemical reaction of ozone with atomic hydrogen. Highly excited molecular oxygen O_2^* in a metastable state is generated from atomic oxygen recombination and can be de-excited by O or O_2, while the $O(^1S)$ and O_2 A-band emissions are radiated from the products. These airglow emissions rely on the atomic oxygen recombination or ozone destruction, and can be recognized as a kind of chemical afterglow. Therefore, they are frequently used as a proxy to retrieve atomic oxygen. More recent measurements were conducted by the Sounding of the Atmosphere using Broadband Emission Radiometry (SABER) instrument on the Thermosphere-Ionosphere-Mesosphere Energetics and Dynamics (TIMED) satellite. The instrument detects OH^* nightglow radiances at 2.0 and 1.6 μm as well as O_3 thermal emissions at 9.6 μm (Smith et al., 2010; Mlynczak et al., 2013b, 2018; Panka et al., 2018). The Scanning Imaging Absorption Spectrometer for Atmospheric CHartographY (SCIAMACHY) instrument on the European Environmental Satellite (Envisat) measures the $O(^1S)$ green line at 557.7 nm and a broad range of OH^* airglow emissions (Kaufmann et al., 2014; Lednyts'kyy et al., 2015; Zhu et al., 2015; Zhu and Kaufmann, 2018). The Optical Spectrograph and Infrared Imager System (OSIRIS) instrument on the Odin satellite probes the O_2 A-band at 762 nm and OH^* airglow at 725–745 nm and 770–815 nm (Sheese et al., 2011, 2014). During the period 1991–1995, the Wind Imaging Interferometer (WINDII) instrument on board the Upper Atmosphere Research Satellite (UARS) also observed the $O(^1S)$ green line and OH(8–3) band emissions at 734 nm(Russell and Lowe, 2003; Russell et al., 2005). Other instruments include the High Resolution Doppler Imager (HRDI) on board UARS, which also observes O_2 A-band emissions (Hays et al., 1993); the Imager of Sprites and Upper Atmospheric Lightning (ISUAL) instrument on board the FORMOSAT-2 satellite, which detects the $O(^1S)$ green line emissions (Gao et al., 2012); and the Solar Mesosphere Explorer (SME) spacecraft, which measures the OH(7–5) band emission at 1.87 μm (Thomas, 1990).

While various datasets are consistent in terms of the overall profile shape of derived [O] densities, some discrepancies still exist (Mlynczak et al., 2013c, a, b; Kaufmann et al., 2014; Mlynczak et al., 2018; Zhu and Kaufmann, 2018; Panka et al., 2018). The radiometric calibration of the instruments or differences in airglow model parameters are potential reasons. Therefore, no common consensus has generally been reached with regard to these aspects. Some new findings on airglow relaxation modeling and reaction kinetic parameters were recently published. A new pathway, in which highly vibrationally excited OH radicals ($v \geq 5$) are deactivated by atomic oxygen to a lower state ($0 \leq v' \leq v\text{-}5$) is proposed and discussed (Sharma et al., 2015; Kalogerakis et al., 2016; Panka et al., 2017, 2018; Fytterer et al., 2019; Kalogerakis, 2019). These results complicate the topic further.

To contribute another piece of information to the currently ongoing discussions, a new dataset derived from the OH nightglow observed by the GOMOS instrument on the Envisat during the years 2002 to 2012 is presented and discussed here. This dataset

is particularly valuable in that it was obtained at the same time as the already published SABER and SCIAMACHY data, but from a different instrument with its own radiometric calibration. Emissions from OH(v=8) are used to obtain atomic oxygen abundances, which is a similar proxy as provided by the SABER and SCIAMACHY OH measurements.

This paper is structured as follows: the second section provides a brief introduction to the instrument and data processing procedure, followed by a section describing the airglow modeling. The derived results are shown in the fourth section, including error analysis as well as latitudinal and temporal analysis. The next section investigates the validation of the dataset in a broad context, including comparisons with the SCIAMACHY dataset and other data sources, while the final section concludes the topic with an outlook on future expectations.

2 Measurements and Data Preparation

2.1 GOMOS on Envisat

The GOMOS (Global Ozone Monitoring by Occultation of Stars) spectrometer is one of nine instruments on board the ESA's (European Space Agency) environmental satellite (Envisat). It is designed to monitor ozone profiles and other entities mostly using stellar occultation and atmospheric transmission measurements in limb-viewing mode (ESA, 2010). Envisat follows a Sun-synchronous orbit with a descending node equator crossing time of 10 p.m. (Gottwald et al., 2011). The operation period of GOMOS dates from April 2002 to April 2012. However, there was an instrument malfunction in summer 2005, resulting in a data gap of nearly three months. The GOMOS instrument delivers one vertical profile of measurements for each occultation, and the altitude coverage spans from 5 km to 150 km, with a vertical sampling rate of better than 2 km (Kyrölä et al., 2012). It has four spectral channels in the ultra-violet to near-infrared spectral range. The spectrometer B2 (SPB2), which provides the data used in this work, covers 925–955 nm with a spectral resolution of 0.13 nm at full width half maximum (FWHM) and a sampling step of 0.056 nm (Massimo Cardaci and Lannone, 2012). The GOMOS detector has three parallel bands. The central band probes the star spectra and the upper/lower bands record the atmospheric background radiation as calibration information, as indicated in Figure 1. The altitudes of tangent points observed by three bands differ roughly by 1.7 km. OH and O_2 A-band are regularly detected in the upper/lower bands, together with auroral lights and the stray light scattered by particles or molecules in the atmosphere. This dataset, which is used in our analysis, is archived in the level-1b limb dataset but not directly utilized in the operational level-2 data retrieval routines. First analyses of the extracted OH and O_2 A-band nightglow measurements from these background datasets were reported by Bellisario et al. (2014).

2.2 Data Selection and Resampling

The GOMOS data were processed with the processor version 6.01–2012. The resulting level-1b limb products have already been geolocated and calibrated (Massimo Cardaci and Lannone, 2012). The signal-to-noise ratio (SNR) of single spectra is on the order of one, and the averaging of data is required for further processing of the data.

Atmos. Chem. Phys. Discuss., https://doi.org/10.5194/acp-2019-417
Manuscript under review for journal Atmos. Chem. Phys.
Discussion started: 13 May 2019

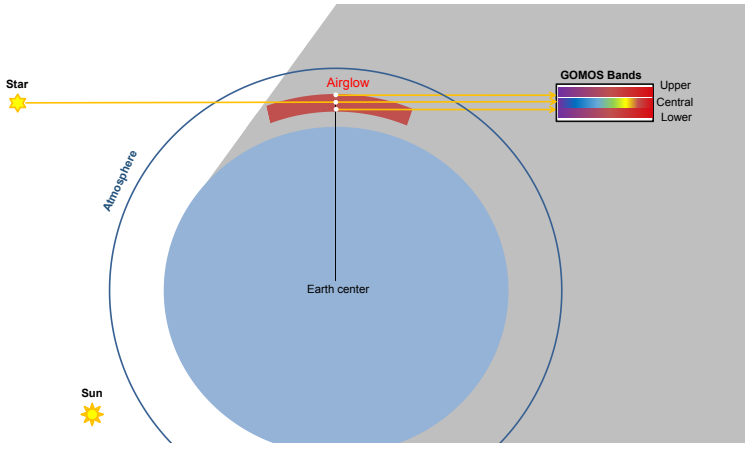

Figure 1. Schematic view of the GOMOS stellar occultation observations. The star transmission spectra are recorded in the central band of the instrument detector, while the atmospheric background radiation is imprinted in the upper/lower bands. The O_2 A-band and OH airglow emissions are detected in the limb observations. For each star spectrum, one upper and one lower spectra are recorded simultaneously.

The raw data from level-1b limb products are first filtered with the corresponding auxiliary "quality flag" and "product confidence data"(PCD), which indicate the presence of bad pixels, saturation, cosmic rays, modulation, dark current, flat-field or vignetting correction, with only data in the normal status being kept. This is then followed by a geolocation-related selection, in which the data with ray-tracing errors are eliminated, and their star IDs and geolocation errors are restricted to within an acceptable range, as recommended by Dehn (2012). The stray light entering the field of view (FOV) of the instrument affects the illumination of the spectrometer and enhances the background noise. The stray light is characterized by the illumination flags and solar zenith angle (SZA) of satellite and tangent points, which are geometrically computed. The illumination conditions of GOMOS measurements are categorized into five flags (Kyrölä et al., 2010; van Gijsel et al., 2010), and the "bright limb" flag thereof is excluded in this work. SZA > 108° is also applied as selection criteria. Near-infrared aurora at wavelengths of around 939 nm and 947 nm, originating from the atomic nitrogen (N I) emissions and N_2^+ Meinel (2–1) band (Baker et al., 1977) are in the spectral range of SPB2. Observations in polar regions are therefore not considered in our analysis.

Due to the nature of the stellar occultation observations, the tangent points of single vertical profiles diverge significantly and are not stationary in latitude-longitude locations. In the level-2 product, they are characterized by the obliquity (Kyrölä et al., 2010), which is not available in the level-1b data. Therefore, in this work, the latitude deviation of tangent points is used instead and profiles with > 4° deviation in tangent point latitudes are disregarded to ensure that every selected profile spans a geographical area of within ±5°.

The archived Level-1b data are signals recorded by the detector, which must be dynamically decoded to electrons and then converted to a physical unit of flux with wavelength-specific radiometric calibration factors. Considering the contamination of star leakage from the central band and residual stray light, which are assumed to be constant with altitude, the averaged spectra from above 110 km are subtracted from each profile as background radiation. No airglow emissions are found above the region

Atmos. Chem. Phys. Discuss., https://doi.org/10.5194/acp-2019-417
Manuscript under review for journal Atmos. Chem. Phys.
Discussion started: 13 May 2019

Atmospheric Chemistry and Physics Discussions

of 110 km in the GOMOS measurements. The subtraction is then followed by the individual "base" removal at each altitude layer, in which this "base" offset is the mean of residual noise of the emission lines. The processed data are resampled into monthly and zonally averaged 10° latitude bins with a fixed altitude grid of 3 km to enhance the spectra SNR and improve retrieval quality. The number of profiles selected for one sample bin (shown in Figure 2) is around 100 to 300 with a large geospatial variation. In order to eliminate the effect of random and systematic noise as well as outliers while retaining as many profiles as possible, the largest and smallest 1 % are disregarded from the measurements at each sample bin for the resampling.

Barrot et al. (2003) reported high pixel response non-uniformity (PRNU) variation of around 12 % in spectrometer B (SPB) during flight. After careful investigation, this was found to arise especially in the wavelength range of 937–950 nm. Therefore, of the entire OH(8–4) band, only the wavelength region of 930–935 nm is utilized in the retrieval to derive the atomic oxygen abundances. It includes three emission lines in the R_1 branch of OH(v=8) with a rotational quantum number of J' = 2.5, 3.5, and 4.5 (illustrated in Figure 3).

The reprocessed spectra are quantified by calculating the standard deviation (STD) of averaged spectra for each sample bin, supplemented by SNR. The calculations show that the mean STD for a typical sample bin in autumn at mid-latitudes is around 2–4$\times 10^9$ photons s^{-1} cm^{-2} nm^{-1} sr^{-1}, and that SNR increases to higher than 10 at peak altitudes and around 3–5 at lower altitudes. A typical profile of processed hydroxyl spectra and integrated radiance are illustrated in Figure 4. Three radiance peaks are clearly recognizable in the spectra (left), while the emission peak layer appears at around 85 km, according to the right-hand side plot.

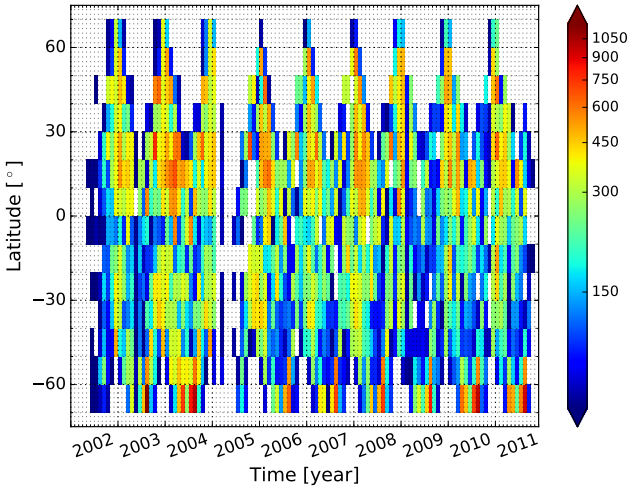

Figure 2. Latitudinal distribution of resampled GOMOS data available from 2002 to 2012. Colour coding indicates the number of selected profiles for each monthly and zonally averaged 10° latitude bin.

Atmos. Chem. Phys. Discuss., https://doi.org/10.5194/acp-2019-417
Manuscript under review for journal Atmos. Chem. Phys.
Discussion started: 13 May 2019

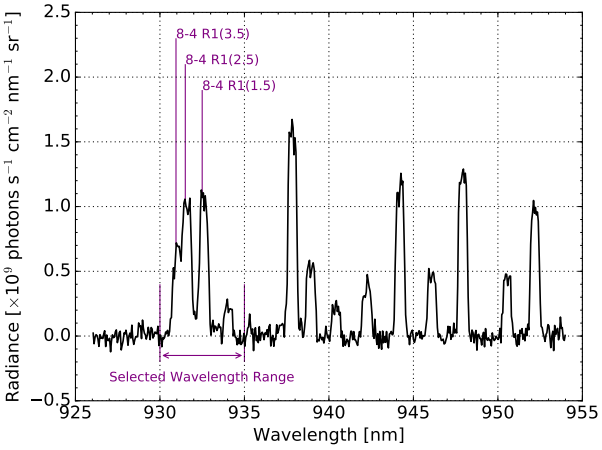

Figure 3. Monthly averaged spectrum for Feb. 2004 is given as an example at 40°–50° N and at an altitude of 89.5 km. The wavelength range from 930 nm to 935 nm is selected and used in the retrieval.

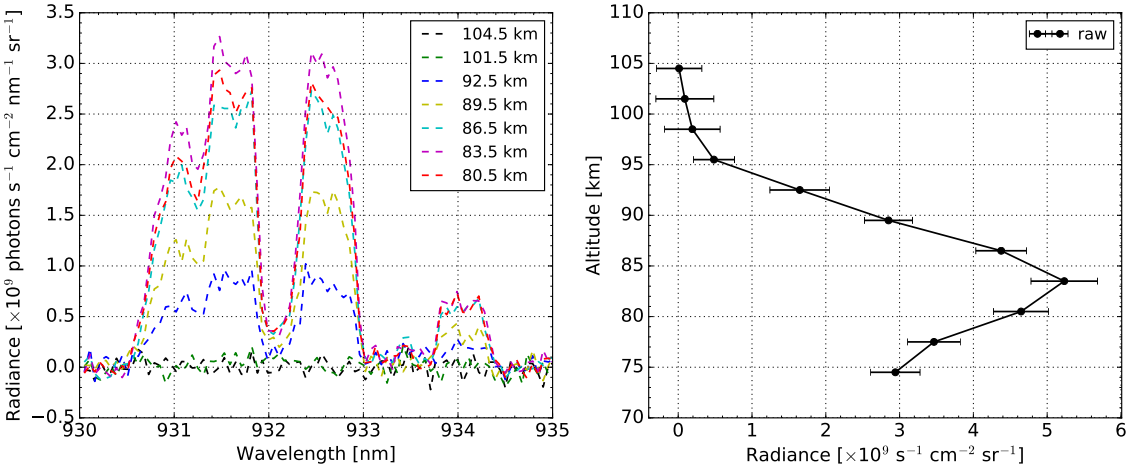

Figure 4. (left) GOMOS monthly zonal mean spectra of OH(8–4) emissions at tangent altitudes as given in the figure legend for Oct. 2003 at 0°–10° S and at a local time of 10–12 p.m.. (right) The spectrally integrated radiance over 930–935 nm versus altitude for the same conditions. The error bars indicate measurement noise, which is computed by integrating the residual noise standard deviation across the spectrum.

3 OH Airglow Modeling and Retrieval Methods

The method to derive atomic oxygen abundance relies on the chemical equilibrium between ozone production and loss during nighttime. It is also applied for the retrieval of atomic oxygen abundances from SABER (Mlynczak et al., 2018) and SCIA-

Atmos. Chem. Phys. Discuss., https://doi.org/10.5194/acp-2019-417
Manuscript under review for journal Atmos. Chem. Phys.
Discussion started: 13 May 2019

MACHY (Zhu and Kaufmann, 2018) OH measurements. Ozone is produced in the three-body recombination reaction of atomic and molecular oxygen. Ozone is destroyed in reactions with atomic hydrogen and oxygen. Most of the model parameters are adopted from Zhu and Kaufmann (2018), and the total removal rate coefficient of OH(v=8) by atomic oxygen is adjusted in such a way that the OH vibrational population density of v=8 is consistent with laboratory measurements (Cosby and Slanger, 2007; Oliva et al., 2015), as summarized in Table 1.

Table 1. OH airglow modeling parameters used in this study, where k_1 to k_3 represent the chemical reaction rate coefficient; f_9 and f_8 refer to the sum of Einstein coefficients of spontaneous transitions from vibrational level v=9 or 8; and k_{N_2}, k_{O_2}, and k_O represent the quenching coefficients of OH^* radicals by N_2, O_2, and O.

Parameter	Process	Rate Constant	Reference
k_1	$O+O_2+M$	$6.0\times10^{-34}(300/T)^{2.4}cm^6s^{-1}$	Sander et al. (2011)
k_2	$H+O_3$	$1.4\times10^{-10}exp(-470/T)cm^3s^{-1}$	Sander et al. (2011)
k_3	$O+O_3$	$8.0\times10^{-12}exp(-2060/T)cm^3s^{-1}$	Sander et al. (2011)
f_9 & f_8	OH^* nascent branching factor	0.47 & 0.34	Adler-Golden (1997)
$k_{N_2(8)}$	$OH(8)+N_2$	$^a1.4\times7\times10^{-13}cm^3s^{-1}$	Adler-Golden (1997)
$k_{O_2(8)}$	$OH(8)+O_2$	$^a1.18\times8\times10^{-12}cm^3s^{-1}$	Adler-Golden (1997)
$k_{O(8)}$	$OH(8)+O$	$6.5\times10^{-11}cm^3s^{-1}$	this work
$k_{O_2(9,8)}$	$OH(9)+O_2\rightarrow OH(8)+O_2$	$^a1.18\times8.9\times10^{-13}cm^3s^{-1}$	this work
$k_{N_2(9)}$	$OH(9)+N_2$	$^a1.4\times(7\pm2)\times10^{-13}cm^3s^{-1}$	Kalogerakis et al. (2011)
$k_{O_2(9)}$	$OH(9)+O_2$	$^a1.18\times(2.2\pm0.6)\times10^{-11}cm^3s^{-1}$	Kalogerakis et al. (2011)
$k_{O(9)}$	$OH(9)+O$	$(2.3\pm1)\times10^{-10}cm^3s^{-1}$	Kalogerakis et al. (2011)

[a] A low temperature scale factor, as the mesopause temperature is normally much lower than the laboratory conditions (Lacoursiére et al., 2003).

Atmospheric background profiles of temperature, total density, and ozone mixing ratio are taken from SABER measurements (v2.0–2016). The same latitude bins ($\pm$ 5°) and local times ($\pm$ 1 hour) were selected for SABER data as GOMOS data. Since SABER cannot measure O_2 and N_2 mixing ratios, these quantities are taken from the mass spectrometer incoherent scatter (MSIS) simulation model data (Picone et al., 2002).

The inverse model applies a constrained global-fit approach following the formalism of Rodgers (2000). The target parameters are the vertical profiles of atomic oxygen abundances, complemented by variables describing the spectral resolution, a wavelength shift, which both are altitude-independent. The content of information in the spectra is sufficient to retrieve these additional parameters. They are capable of reproducing the spectrum characteristics, which cannot be fully captured only by regulating oxygen densities in the model, thus resulting in a better agreement between measured and simulated spectra. Besides, the a priori information from the real atmospheric state is considered as the regularization term for the retrieval. The Tikhonov regularization matrix (Tikhonov and Arsenin, 1977) is therefore included and accordingly adjusted so that the influence of measurement noise is minimized and the results are constrained in a physically reasonable domain.

Atmos. Chem. Phys. Discuss., https://doi.org/10.5194/acp-2019-417
Manuscript under review for journal Atmos. Chem. Phys.
Discussion started: 13 May 2019

Atmospheric Chemistry and Physics Discussions

4 Results

4.1 Atomic Oxygen Abundances

Applying the global fitting method to GOMOS level-1b limb products, a globally distributed longtime series [O] dataset is derived, along with other quantities. The fitted spectra are compared with the measurements as shown in Figure 5 (left). In general, they are in good agreement. The spectrally integrated radiances in Figure 5 (right) also show consistency. The typical value of retrieved spectral resolution is around 0.48 nm, and no wavelength shift is found. The derived oxygen densities are within an altitude range of 80 km to 100 km, covering the period from May 2002 to December 2011 and spanning local times from 10:00 p.m. to 12:00 p.m.. A typical atomic oxygen profile is shown in Figure 6 with a maximum concentration of about 3.5×10^{11} atoms cm^{-3} at 95 km. Above the maximum, there is a downward flux of atomic oxygen by diffusive transport (Swenson et al., 2018). Turbulences associated with gravity wave breaking, along with damped waves or tides, are the dynamic processes that contribute to this diffusive transport (Smith et al., 1987; Li et al., 2005). Below the maximum, there is a rapid decrease in atomic oxygen density, which is mainly due to the vertical transport and chemical losses. At an altitude of around 85 km, atomic oxygen density already declines by one order of magnitude to 10^{10} atoms cm^{-3}.

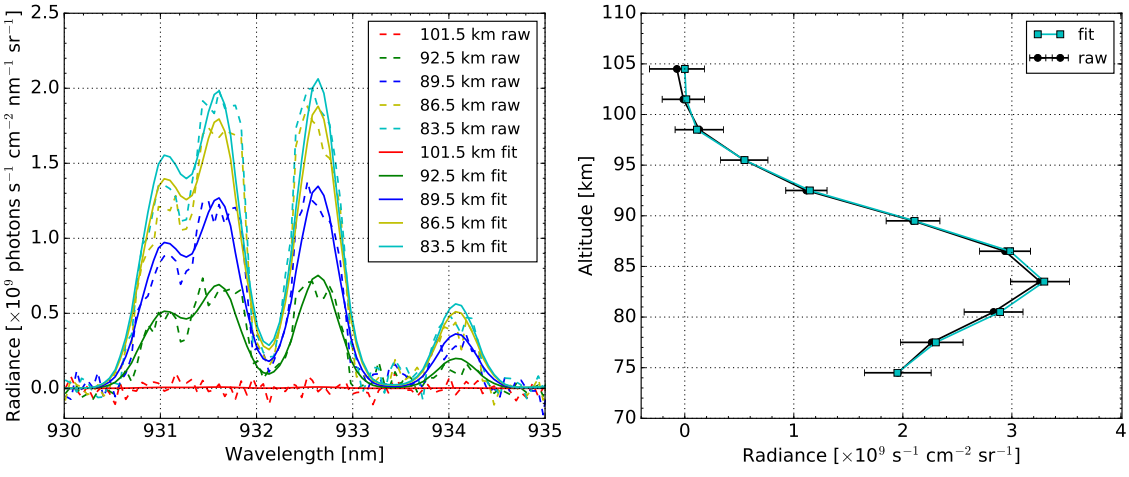

Figure 5. (left) Simulated spectra (solid line) and measurements (dashed line) of GOMOS monthly zonal mean measurements of OH(8–4) airglow emissions at tangent altitudes, as given in the figure legend for Feb. 2006 at 10°–20° N and a local time of 10–12 p.m.. (right) The spectrally integrated radiance over 930–935 nm versus altitude for the same conditions.

4.2 Error Analysis

The accuracy of the derived atomic oxygen densities not only depends on the measurement noise, but also the smoothing error as well as the uncertainties in forward model parameters and the background atmosphere input. The largest source of uncertainties is found in the forward model parameters. The chemical reaction rate coefficient k_1 has an uncertainty of around

Atmos. Chem. Phys. Discuss., https://doi.org/10.5194/acp-2019-417
Manuscript under review for journal Atmos. Chem. Phys.
Discussion started: 13 May 2019

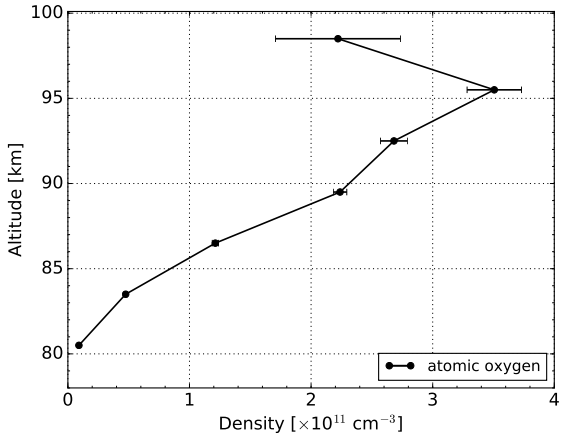

Figure 6. Atomic oxygen abundances, derived from GOMOS monthly zonal mean measurements of OH(8–4) airglow emissions for Feb. 2006 at 10°–20° N. The error bar represents the statistical uncertainty coming from the measurement noise. It increases towards higher altitudes, as a consequence of the corresponding SNR being lower.

20 %, contributing around 15 % uncertainty below 90 km and around 20 % at 95 km in derived abundances. k_3 introduces an increasing uncertainty of up to 6 % at 95 km. The nascent branching factor (e.g. f_8, f_9) explains the distribution ratio of excited hydroxyl radicals OH^* of different vibrational levels. f_8 has a linear influence on the uncertainty of the results; a perturbation of 10 % on its values results in a similar retrieval uncertainty. The errors of Einstein coefficients correspond to an uncertainty of around 7 % in the results. The quenching coefficient $k_{O_2(8)}$ of OH^* radicals with oxygen molecules corresponds to an uncertainty of 5 %, and the influences of other model parameters are in the order of 1–2 % or less. SABER temperature uncertainties are the predominant factor influencing the retrieval results in the background atmosphere. The uncertainties are around 5.5 K at 80 km and increase to 13 K at 90 km (Dawkins et al., 2018). This could lead to an uncertainty of 5 % below 90 km and up to 20 % above 95 km, taking into account the compensation effects of total density changes following the hydrostatic equilibrium (Zhu and Kaufmann, 2018).

At the altitude of 80–100 km, the effects of the smoothing error and measurement noise on the uncertainty are on the order of around 0.5 % and 5 %, respectively. It is due to a properly chosen regularization in the retrieval procedure that the a priori information is negligible in the retrieval results. As part of a more in-depth look into the retrieval results, the average kernel and vertical resolution are investigated, as shown in Figure 7. The total average kernels in the altitude region of interest (80–100 km) are equal to one, indicating that the measurements instead of the a priori information contribute to nearly all of the retrieval result. The peaks of average kernels are found at tangent altitudes and the corresponding vertical resolution for each altitude is around 3 km. It is consistent with the input altitude grid of 3 km, referring to the retrieval information mainly originates from the atmospheric state of the tangent point and is strictly constrained in the proximately vertical sampling grid of 3 km.

Atmos. Chem. Phys. Discuss., https://doi.org/10.5194/acp-2019-417
Manuscript under review for journal Atmos. Chem. Phys.
Discussion started: 13 May 2019

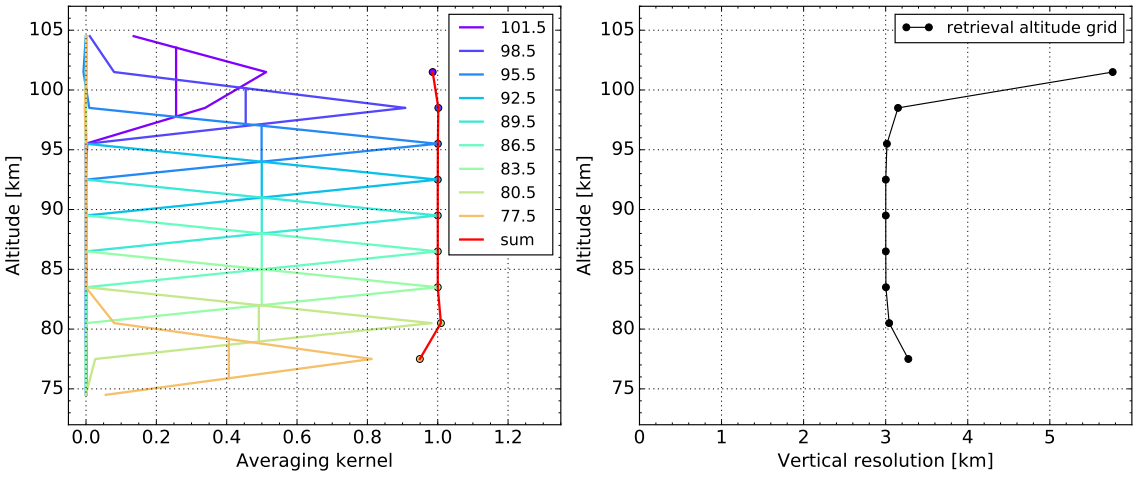

Figure 7. (left) The average kernel and (right) the vertical resolution of the retrieval for Feb. 2006 at 10°–20° N and a local time of 10–12 p.m.. The retrieval altitude grid refers to the vertical resolution of the derived quantities and is equal to the FWHM of average kernels in the corresponding altitude layers.

4.3 Spatial and Temporal Analysis

Atomic oxygen reveals a two-cell structure at mid-latitudes, which is most pronounced during the equinox seasons (Figure 8). The smallest values appear over the equatorial region and the largest values are at mid-latitudes. As already mentioned and discussed by Smith et al. (2010), this latitudinal distribution structure of atomic oxygen is influenced by local time dependent migrating diurnal tides, which have a maximum wind amplitude over the equator and two weaker maxima of opposite signs at mid-latitudes. At a local time of almost midnight, the atomic oxygen displacement is upward at the equator (resulting in an [O] decrease) and downward in subtropical latitudes (resulting in an [O] enrichment).

In Figure 9, a vertical distribution comparison of derived densities from 2002 to 2011 over the mid-latitude and equatorial regions is shown. Both the annual oscillation (AO) and semiannual oscillation (SAO) can be seen from the temporal evolution of mid and lower latitudes. The SAO reaches its maximum at equinox seasons, which is related to the semiannual variation of the atmospheric tide amplitudes (Smith et al., 2010).

A multiple linear regression analysis is applied to quantitatively analyze the longtime variations of the GOMOS [O] dataset. The monthly mean column density integrated from 80–97 km for 20°–30° N is analyzed by the harmonic fitting, which includes components such as the solar cycle effect, SAO, AO and QBO (quasi biennial oscillation), and offset.

$$[O]_{Column} = Offset + A_{solar} \cdot I_{solar} \cdot (t + shift) + A_{SAO} \cdot cos(\frac{2\pi t}{6} + P_{SAO}) \quad (1)$$

$$+ A_{AO} \cdot cos(\frac{2\pi t}{12} + P_{AO}) + A_{QBO} \cdot cos(\frac{2\pi t}{27.5} + P_{QBO}) \quad (2)$$

Atmos. Chem. Phys. Discuss., https://doi.org/10.5194/acp-2019-417
Manuscript under review for journal Atmos. Chem. Phys.
Discussion started: 13 May 2019

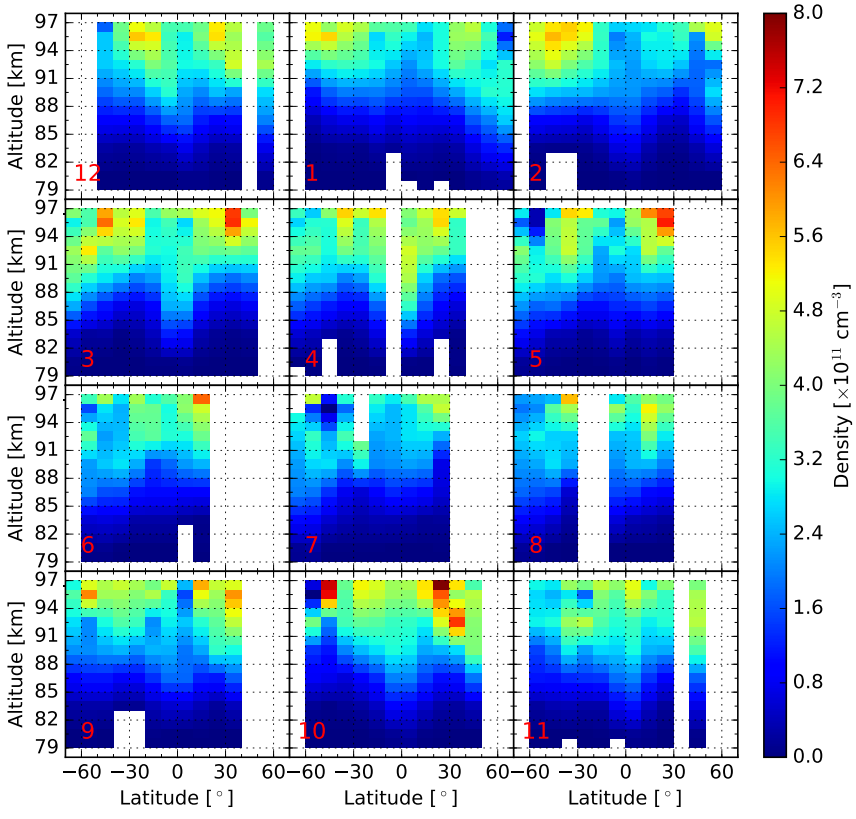

Figure 8. Latitude-altitude distribution of the zonal mean atomic oxygen density for 2007. Each row represents approximately a season. The data are linearly interpolated into a 1 km altitude grid for better illustration. The numbers in the subplots indicate the month of the year.

The variable t represents the month since 2002 and the column density is fitted by amplitudes (A, atoms cm^{-3}) and phase shifts (P) of SAO (period of 6 months), AO (period of 12 months), and QBO (period of 27.5 months), complemented by the amplitude and shift of the 11-year solar cycle effect, as well as an offset. The coefficient I_{solar} is the solar radio flux ($F_{10.7}$ cm) taken from Tapping (2013). Typical mesospheric QBO (MQBO) period is reported approximately 27.5 months by investigating mesospheric zonal wind measurements (Ratnam et al., 2008; de Wit et al., 2013; Malhotra et al., 2016), therefore a period of 27.5 months is considered for the QBO component in this analysis. The non-linear least squares fitting method (Levenberg–Marquardt algorithm) is applied to derive these fitting parameters, as described in detail by Kaufmann et al. (2013) and Zhu et al. (2015).

In Figure 10, the raw data and fitting results are illustrated, along with the linear fitting, considering only the first two components in the equation. The [O] longtime variations are well characterized by the fit. The 11-year solar cycle effect

Atmos. Chem. Phys. Discuss., https://doi.org/10.5194/acp-2019-417
Manuscript under review for journal Atmos. Chem. Phys.
Discussion started: 13 May 2019

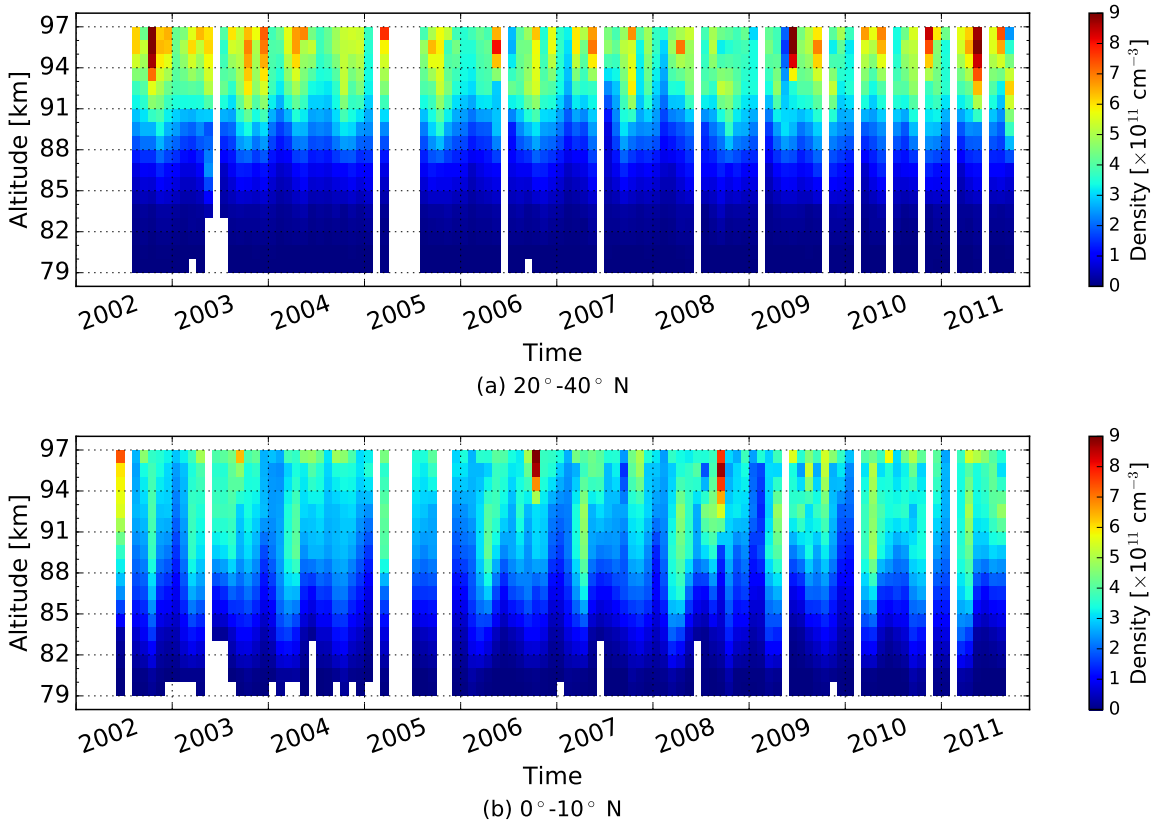

Figure 9. Temporal evolution of the vertical distribution of atomic oxygen densities for 20°–40° N (a) and 0°–10° N (b). The data are linearly interpolated into a 1 km altitude grid.

is captured, in which the atomic oxygen density is 17.1 % smaller in 2008/2009 (minimum of solar cycle 23/24) than in 2002/2011 (near solar maximum conditions of solar cycles 23 & 24), due to different radiative forcing conditions during the solar cycles. The atomic oxygen abundance difference of 17.1 % under solar min/max conditions agrees with model investigations and experimental results, which are normally in a range of around 10 % to 30 % (Schmidt et al., 2006; Marsh et al., 2007; Kaufmann et al., 2014; Zhu et al., 2015). A significant semiannual oscillation is observed, reaching a maximum in equinox seasons, which is in agreement with the analysis above, and the amplitude is about 18 %. The annual oscillation has an amplitude of 9.6 %, with the maximum being reached near summer solstices and the minimum near winter solstices. These results are consistent with the analyses of Zhu et al. (2015) and Lednyts'kyy et al. (2017), which reported SAO amplitudes on the order of 15 % and 12 %, AO amplitude of 11 % and 7 %, respectively. The QBO amplitude is in the order of 1.7 %. The multiple linear fitting analyses on other latitudinal bands and altitudes also show a similar solar cycle effect as well as AO and SAO variations, as some examples are summarized in Table 2.

Atmos. Chem. Phys. Discuss., https://doi.org/10.5194/acp-2019-417
Manuscript under review for journal Atmos. Chem. Phys.
Discussion started: 13 May 2019

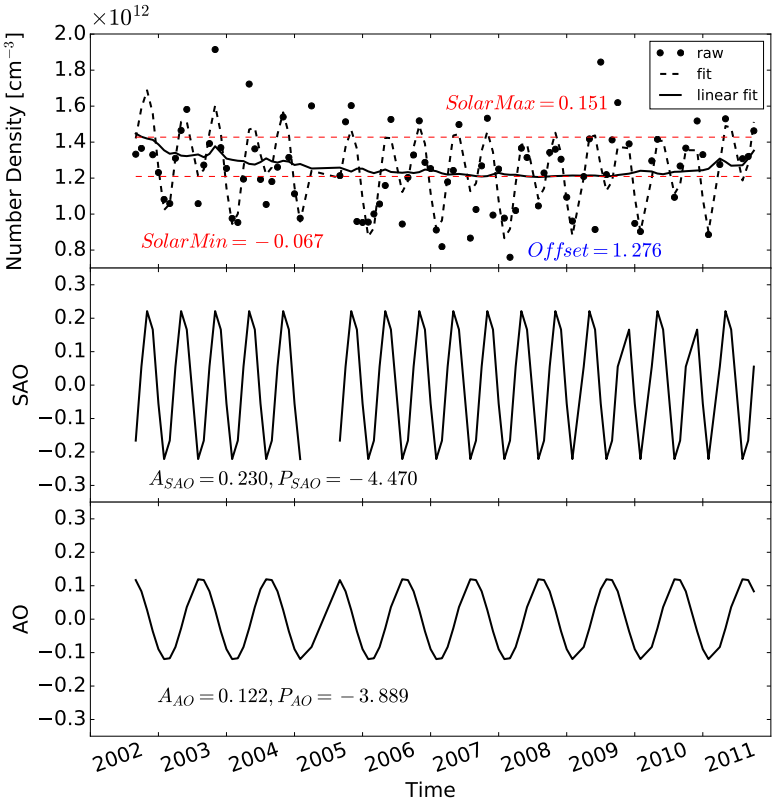

Figure 10. Multiple linear regression analysis of vertically integrated, monthly mean atomic oxygen densities of 80–97 km for 20°–30° N from 2002 to 2011. (upper panel) The raw and fitted data are shown along with the linear fit, which represents the constant offset plus the linear solar flux component in the multiple linear regression results. (middle) SAO and (lower) AO parts are also illustrated with corresponding parameters. A_{SAO}, P_{SAO}, A_{AO}, and P_{AO} are the amplitudes and phase shifts of SAO and AO, respectively. The quantities of SolarMin, SolarMax, Offset and amplitudes are in unit of 10^{12} atoms cm^{-3}. The gap present in the SAO is caused by the data discontinuity.

Table 2. Summary of multiple linear regression analysis results of monthly mean atomic oxygen column densities integrated over 80–97 km for 20°–30° N, 0°–10° N, and 30°–20° S from 2002 to 2011. The quantities are in unit of 10^{12} atoms cm^{-3}. A_{SAO}, A_{AO}, and A_{QBO} are the amplitudes of SAO, AO, and QBO, respectively.

Latitude bin	Offset	Solar Max	Solar Min	A_{SAO}	A_{AO}	A_{QBO}
20°–30° N	1.276	0.151	-0.067	0.23	0.122	0.022
0°–10° N	1.221	0.085	-0.044	0.272	0.126	0.05
30°–20° S	1.126	0.097	-0.052	0.183	0.074	0.025

Atmos. Chem. Phys. Discuss., https://doi.org/10.5194/acp-2019-417
Manuscript under review for journal Atmos. Chem. Phys.
Discussion started: 13 May 2019

Atmospheric Chemistry and Physics Discussions

5 Discussion

5.1 Validation by SCIAMACHY Data

The SCIAMACHY instrument, another limb sounder on board the Envisat satellite, observed OH emissions at various wavelengths from visible to infrared emissions (Bovensmann et al., 1999; Kaufmann et al., 2008). This provides us with the best opportunity for a comprehensive joint investigation of the GOMOS [O] dataset, as SCIAMACHY covers exactly the same OH(8–4) band wavelengths as GOMOS. Two more datasets of [O] derived from SCIAMACHY green line emissions and OH(9–6) band airglow are currently available.

SCIAMACHY performed the OH airglow measurements in dark limb-viewing mode in the flight direction, with the recorded spectra always at a local solar time of 10 p.m. and a fixed altitude grid of 3.3 km. The OH(8–4) band observation is located in Channel 5 with a spectral resolution of 0.54 nm. SCIAMACHY data Version 8–2016 is adopted in this work. A continuous observation was performed during the entire lifetime of Envisat. The number of recorded profiles in one sample bin was around 100–300 before 2005 and significantly increased to 400–600 because of a change in instrument operations. SNRs of single profiles are normally on the order of 6 at peak altitudes and decrease to 1 at lower altitudes. After monthly zonal averaging, SNRs increase by one order of magnitude, and the mean noise level is around 0.6×10^9 photons s^{-1} cm^{-2} nm^{-1} sr^{-1}.

Theoretically, the SCIAMACHY and GOMOS measurements should be identical in the same wavelength range of OH airglow emissions. In practice, however, due to effects of various factors, such as instrument characteristics and radiometric calibration, they do not fully conform with each other in terms of absolute radiance or instrument line shapes. In this study, the two data products are found to be consistent in terms of absolute radiance within $\pm$ 20 % in the peak emissions layer (shown in Figure 11), after monthly zonal averaging. One specific example of spectra comparison is given in Figure 12. The emission radiances from two data products are similar, but the GOMOS spectra are more noisy. The atomic oxygen abundances derived from this example bin is given in Figure 13 (b).

The same retrieval procedure is applied to the SCIAMACHY data. The differences between the atomic oxygen abundances from the two instruments are illustrated in Figure 14. There are no major systematic discrepancies and they agree within a $\pm$ 20 % difference in most latitude-altitude bins as expected from the differences of the corresponding radiances. The GOMOS data is found to be over 20 % lower in the northern hemisphere in February, and also in tropical regions in March, May, and September. GOMOS values appear to be 20 % larger at low altitudes of around 80 km in some scattered bins. In general, these two atomic oxygen datasets derived from OH(8–4) airglow emissions are consistent with each other in the context of absolute abundances.

A comparison of the GOMOS data with atomic oxygen obtained from SCIAMCHY OH(9–6) emissions (Zhu and Kaufmann, 2018) is given in Figure 13 for different latitudinal and seasonal conditions. The absolute abundances of the three datasets are in the same order of magnitude and they agree with each other at the altitude region of interest of 80–95 km. Specifically, atomic oxygen abundances derived from OH(v=8) emissions by both instruments are found to be around 10 % lower than those derived from OH(v=9) at around 90 km. This might be explained by a slight underestimation of the quenching of OH(v=9) to

Atmos. Chem. Phys. Discuss., https://doi.org/10.5194/acp-2019-417
Manuscript under review for journal Atmos. Chem. Phys.
Discussion started: 13 May 2019

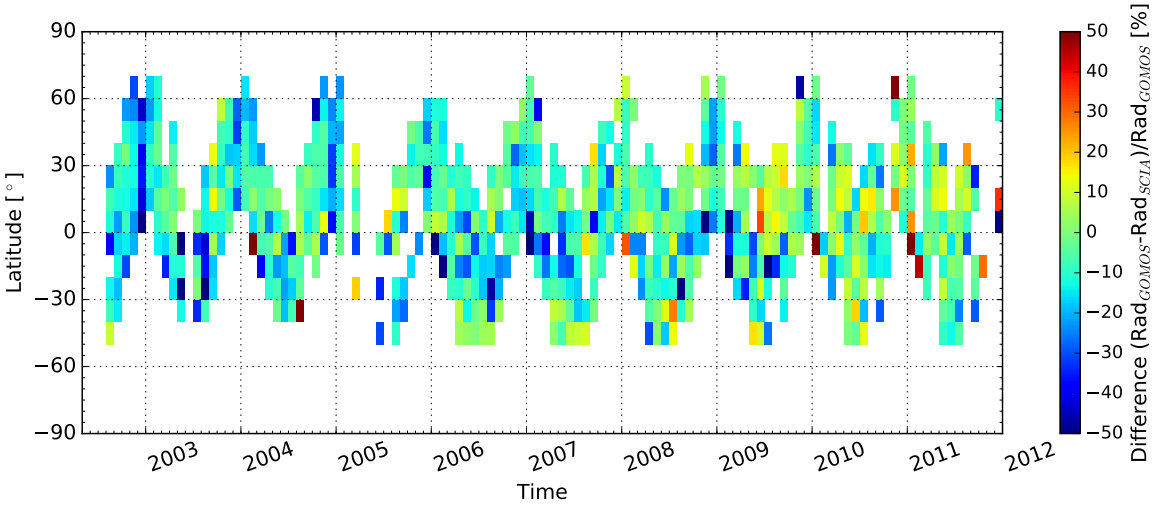

Figure 11. Temporal evolution of radiance differences (in percentage) between GOMOS and SCIAMACHY at an altitude of 86.5 km. The radiance is integrated over the wavelength of 930–935 nm. Negative numbers indicate that SCIAMACHY radiances are larger than those of GOMOS.

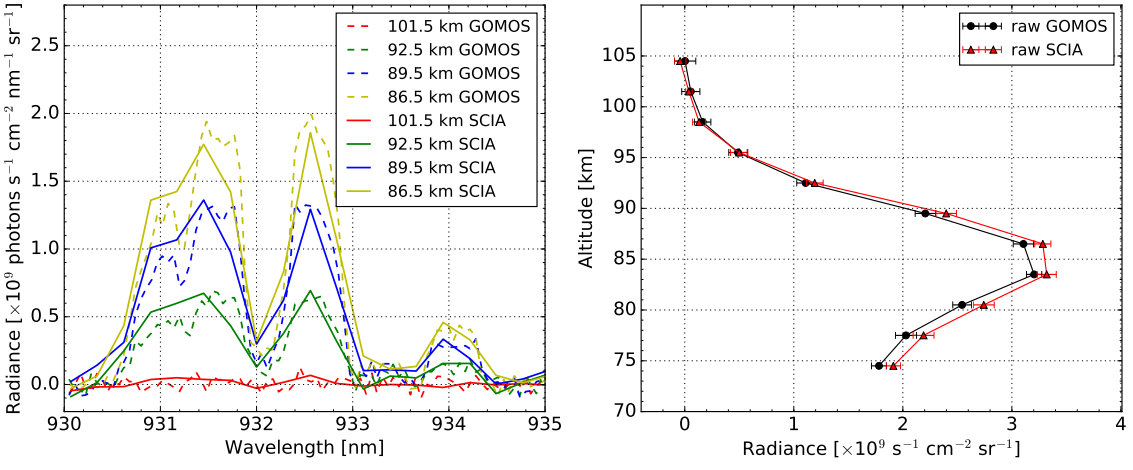

Figure 12. (left) SCIAMACHY (solid line) and GOMOS (dashed line) observations of monthly zonal mean OH(8–4) airglow emissions at the tangent altitudes, as given in the Figure legend for Apr. 2004 at 20°–30° N and a local time of 10–12 p.m. (right) The spectrally integrated radiance over 930–935 nm versus altitude for the same conditions. The error bars are measurement noise, computed as in Figure 4.

OH(v=8) by O_2, an overestimation of the deactivation of OH(v=8) due to collisions with atomic or molecular oxygen, or the over/under-estimation of the branching factors f_9 and f_8 in the OH airglow model.

Atmos. Chem. Phys. Discuss., https://doi.org/10.5194/acp-2019-417
Manuscript under review for journal Atmos. Chem. Phys.
Discussion started: 13 May 2019

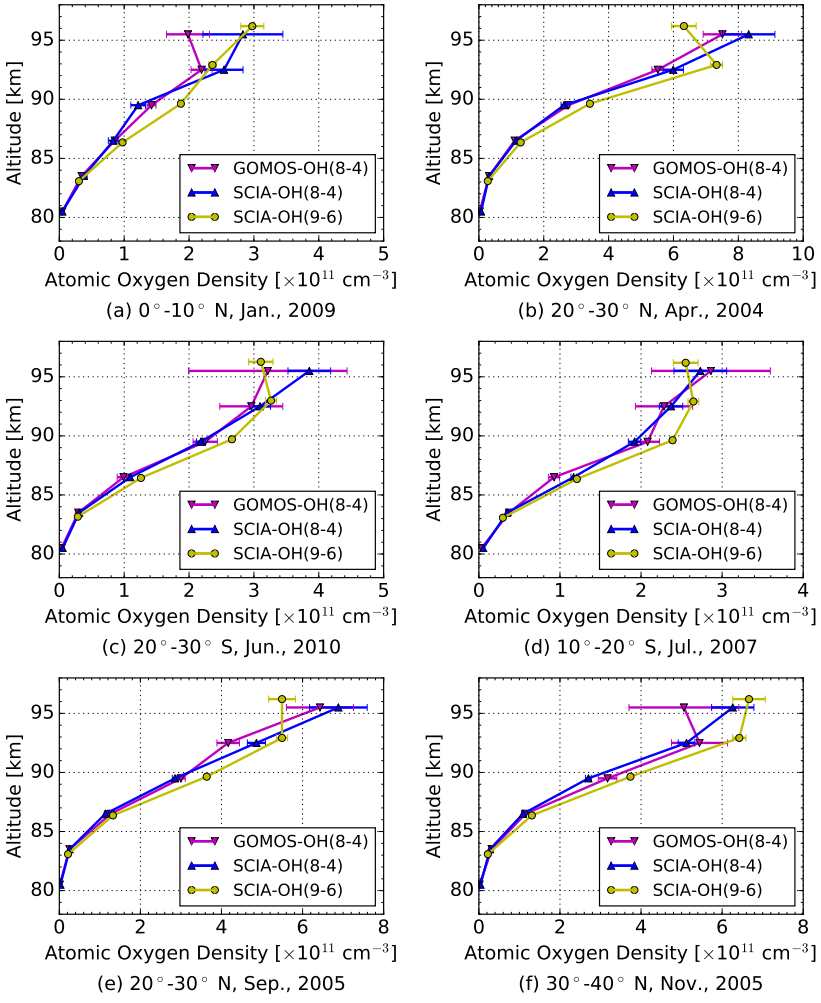

Figure 13. Comparison of monthly zonal mean atomic oxygen densities derived from hydroxyl airglow emissions observed by the GOMOS and SCIAMACHY instruments in various latitude bins for different months. SCIA-OH(9–6) represents the atomic oxygen dataset derived from the SCIAMACHY OH(9–6) band by Zhu and Kaufmann (2018); SCIA-OH(8–4) is the dataset from the SCIAMACHY OH(8–4) band; and GOMOS-OH(8–4) is from the GOMOS measurements of the OH(8–4) band.

5.2 Comparison with Other Datasets

There are a number of O_2 and O excited states, which can also be used as proxies for atomic oxygen. This includes O(^{1}S) green line and O_2 A-band emissions. Their modeling is mostly independent from the calculation of OH(v) emissions, although some processes have to be considered in all models. Rocket-borne in situ measurements of atomic oxygen are the most independent from methods based on nightglow. Mostly performed in the 1970s (Offermann et al., 1981), the measurements are very rare and selective. Figure 15 gives an impression of how the various datasets of atomic oxygen available in the literature fit to each

Atmos. Chem. Phys. Discuss., https://doi.org/10.5194/acp-2019-417
Manuscript under review for journal Atmos. Chem. Phys.
Discussion started: 13 May 2019

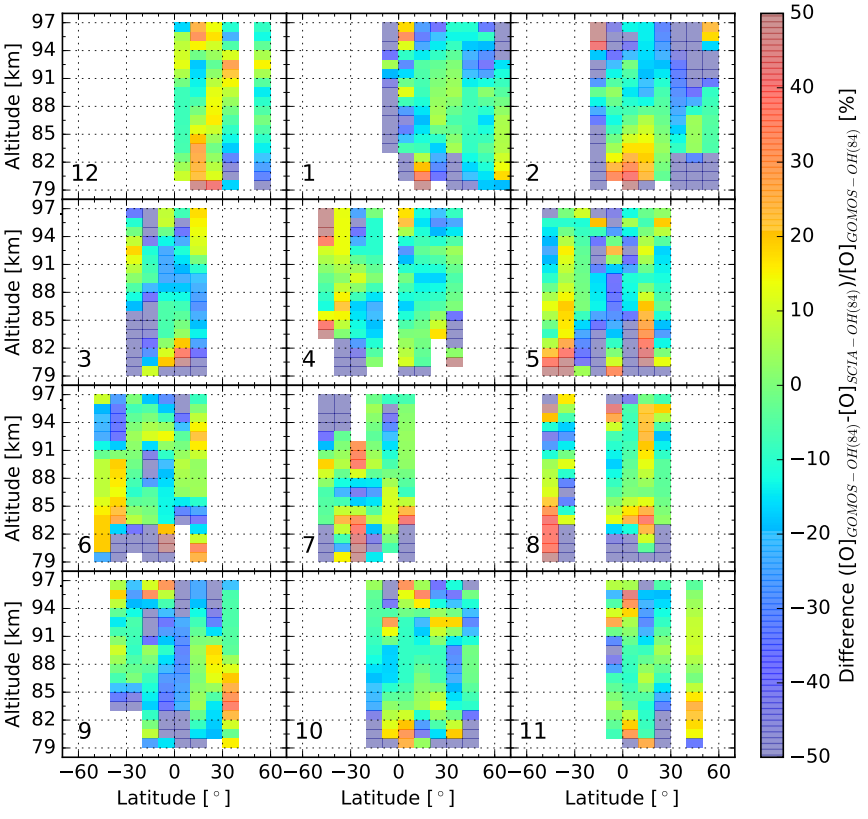

Figure 14. Latitude-altitude distribution of percentage differences between zonal mean atomic oxygen densities derived from GOMOS and SCIAMACHY OH(8–4) airglow emissions for 2007. Each row represents approximately a season. Negative numbers indicate that SCIAMACHY abundances are larger than those obtained from GOMOS. The data are linearly interpolated into a 1 km altitude grid. The numbers in the subplots indicate the month of the year.

other. All the sets are selected using a similar local time of around 10–11 p.m., with the exception of OSIRIS (6:30 p.m.) and in situ data with diverse local times at midnight or in the afternoon.

The datasets agree within their combined uncertainties in most cases. The absolute abundances are typically 4–6$\times 10^{11}$ atoms cm^{-3} above 90 km and decrease with descending altitudes by one order of magnitude (at around 80 km) for mid-latitude in autumn. GOMOS data are around 10 % lower than SCIAMACHY-O(^{1}S) and both SABER-OH datasets at 90–95 km, but remain in good agreement with these datasets at lower altitudes below 90 km. The OSIRIS dataset appears as the lower bound of the values above 90 km, as it is always the lowest in this region, while it becomes relatively large below 90 km. The WINDII dataset is around 10 % lower than the GOMOS-OH data at an altitude of 87–92 km, but they generally fit to each other. In

Atmos. Chem. Phys. Discuss., https://doi.org/10.5194/acp-2019-417
Manuscript under review for journal Atmos. Chem. Phys.
Discussion started: 13 May 2019

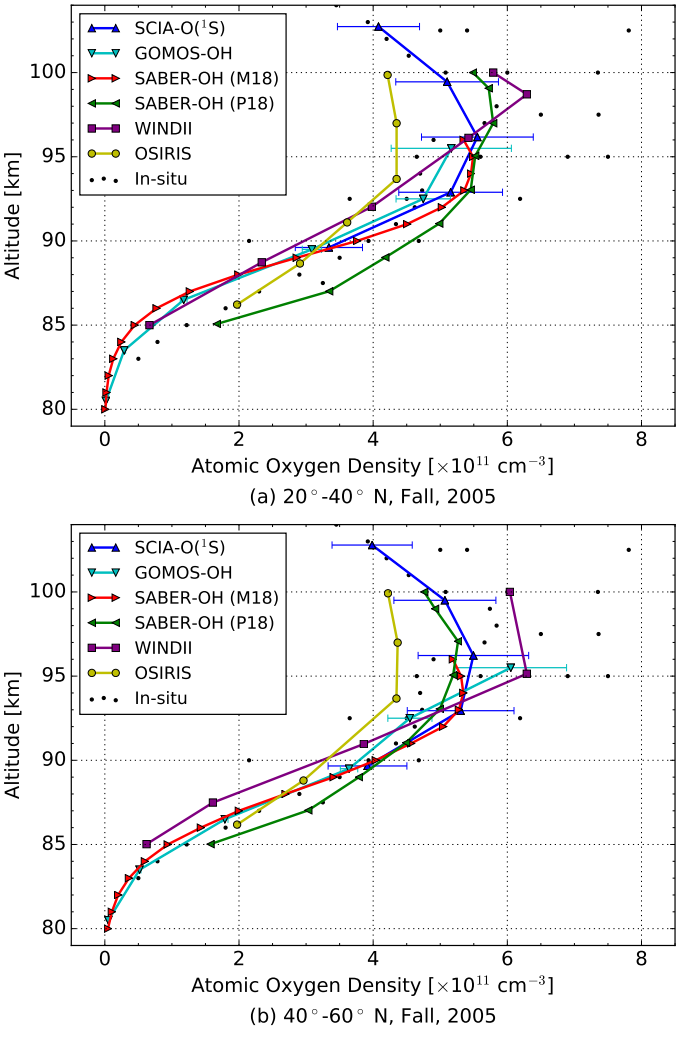

Figure 15. Comparison of derived atomic oxygen densities derived from various instruments and measurement techniques averaged for 20°–40° N (a) and 40°–60° N (b) in autumn (Sep., Oct., Nov.), 2005. SCIA-O(^{1}S) is the atomic oxygen data derived from SCIAMACHY green line emissions (Kaufmann et al., 2014; Zhu et al., 2015); SABER-OH refers to the atomic oxygen datasets derived by Mlynczak et al. (2018) (M18); and Panka et al. (2018) (P18) from SABER hydroxyl airglow emissions. The WINDII dataset is obtained from WINDII combined hydroxyl and green line observations, 1993 (Russell and Lowe, 2003; Russell et al., 2005), while the OSIRIS dataset is derived from OSIRIS O_2 A band measurements (Sheese et al., 2011). In situ data are obtained from rocket-borne experiments with mass spectrometers, conducted at different local times at 37–40° N, from 1972 to 1976 (Offermann and Grossmann, 1973; Trinks et al., 1978; Offermann et al., 1981).

situ data scatter in a large variation, which might be caused by the diurnal tides (local time differences), and the GOMOS-OH dataset is still located in its overall range of spread.

6 Conclusions

GOMOS limb observations of the background atmosphere provide the opportunity to retrieve atomic oxygen abundances from hydroxyl nightglow emissions at the mesopause. A global night-time [O] dataset is obtained by applying the OH modeling and retrieval method to the monthly zonal mean of GOMOS limb measurements. Its uncertainty comes from the measurement noise (around 5 %), selected relaxation schemes and kinetic parameters in OH modeling (contributing around 20 % in total) and background atmosphere inputs, for example atmospheric temperature, ozone (around 5 % to 20 %). The obtained profiles present an overall picture of the vertical distribution of atomic oxygen from 80 km to 100 km. A temporal analysis of the profiles shows 11-year solar cycle effect tendencies as well as semiannual and annual variations, of which SAO is the most prominent.

The GOMOS data agrees with the SCIAMACHY OH(8–4) measurements, with deviations typically smaller than 20 %. They are, on average, about 10 % lower than atomic oxygen data obtained from SCIAMACHY OH(9–6) observations. This might indicate that the collisional energy exchange between OH(v=9) and OH(v=8) via collisions with O_2 and O in the OH airglow model requires some readjustments.

Data availability. The GOMOS and SCIAMACHY data used in this study are available to the public at ftp://eoa-dp.eo.esa.int as part of the Cat-1 project 2515. SABER Version 2.0 can be downloaded from http://saber.gats-inc.com. Derived atomic oxygen datasets are available on request.

Author contributions. QC processed the data, performed the analysis and drafted the manuscript. MK and YZ initiated the topic, provided insight and instructions, and discussed the results regularly. All authors contributed to the revision and improvement of the paper.

Competing interests. The authors declare that they have no conflict of interest.

Acknowledgements. Q. Chen was supported in her work by the China Scholarship Council. The work of Y. Zhu was supported by the 2017 Helmholtz–OCPC Programme and the International Postdoctoral Exchange Fellowship Program 2017.

References

Adler-Golden, S.: Kinetic parameters for OH nightglow modeling consistent with recent laboratory measurements, Journal of Geophysical Research: Space Physics, 102, 19 969–19 976, https://doi.org/10.1029/97JA01622, https://agupubs.onlinelibrary.wiley.com/doi/abs/10.1029/97JA01622, 1997.

Baker, D., Pendleton Jr., W., Steed, A., Huppi, R., and Stair Jr., A. T.: Near-infrared spectrum of an aurora, Geophysical Research Letters, 82, 1601–1609, https://doi.org/10.1029/JA082i010p01601, https://agupubs.onlinelibrary.wiley.com/doi/abs/10.1029/JA082i010p01601, 1977.

Barrot, G., Bertaux, J.-L., Fraisse, R., and Mangin, A.: GOMOS calibration on Envisat-status on December 2002, in: Proc. of Envisat Validation Workshop, 2003.

Bellisario, C., Keckhut, P., Blanot, L., Hauchecorne, A., and Simoneau, P.: O_2 and OH Night Airglow Emission Derived from GOMOS-Envisat Instrument, Journal of Atmospheric and Oceanic Technology, 31, 1301–1311, https://doi.org/10.1175/JTECH-D-13-00135.1, https://hal.archives-ouvertes.fr/hal-00968748, 2014.

Bovensmann, H., Burrows, J. P., Buchwitz, M., Frerick, J., Noël, S., Rozanov, V. V., Chance, K. V., and Goede, A. P. H.: SCIAMACHY: Mission Objectives and Measurement Modes, Journal of the Atmospheric Sciences, 56, 127–150, https://doi.org/10.1175/1520-0469(1999)056<0127:SMOAMM>2.0.CO;2, 1999.

Brasseur, G. and Offermann, D.: Recombination of atomic oxygen near the mesopause: Interpretation of rocket data, Journal of Geophysical Research: Atmospheres, 91, 10 818–10 824, https://doi.org/10.1029/JD091iD10p10818, https://agupubs.onlinelibrary.wiley.com/doi/abs/10.1029/JD091iD10p10818, 1986.

Brasseur, G. P. and Solomon, S.: Aeronomy of the Middle Atmosphere: Chemistry and Physics of the Stratosphere and Mesosphere, vol. 32 of *Atmospheric and Oceanographic Sciences Library*, Springer Netherlands, 3 edn., 2005.

Cosby, P. C. and Slanger, T. G.: OH spectroscopy and chemistry investigated with astronomical sky spectra, Canadian Journal of Physics, 85, 77–99, https://doi.org/10.1139/p06-088, https://doi.org/10.1139/p06-088, 2007.

Dawkins, E. C. M., Feofilov, A., Rezac, L., Kutepov, A. A., Janches, D., Höffner, J., Chu, X., Lu, X., Mlynczak, M. G., and Russell III, J.: Validation of SABER v2.0 Operational Temperature Data With Ground-Based Lidars in the Mesosphere-Lower Thermosphere Region (75-105 km), Journal of Geophysical Research: Atmospheres, 123, 9916–9934, https://doi.org/10.1029/2018JD028742, https://agupubs.onlinelibrary.wiley.com/doi/abs/10.1029/2018JD028742, 2018.

de Wit, R. J., Hibbins, R. E., Espy, P. J., and Mitchell, N. J.: Interannual variability of mesopause zonal winds over Ascension Island: Coupling to the stratospheric QBO, Journal of Geophysical Research: Atmospheres, 118, 12,052–12,060, https://doi.org/10.1002/2013JD020203, https://agupubs.onlinelibrary.wiley.com/doi/abs/10.1002/2013JD020203, 2013.

Dehn, A.: Quality Readme File for GOMOS Level 1b data version GOMOS/6.01, Tech. Rep. ENVI-GSOP-EOGD-QD-12-0116, European Space Agency, 2012.

Dickinson, P. H. G., Bolden, R. C., and Young, R. A.: Measurement of atomic oxygen in the lower ionosphere using a rocket-borne resonance lamp, Nature, 252, pages 289–291, https://doi.org/https://doi.org/10.1038/252289a0, 1974.

Dickinson, P. H. G., Bain, W. C., Thomas, L., Williams, E. R., Jenkins, D. B., and Twiddy, N. D.: The Determination of the Atomic Oxygen Concentration and Associated Parameters in the Lower Ionosphere, Proceedings of the Royal Society of London. Series A, Mathematical and Physical Sciences, 369, 379–408, http://www.jstor.org/stable/2398309, 1980.

ESA: European space agency-Envisat GOMOS Product Handbook, http://envisat.esa.int/handbooks/gomos/CNTR.html, [Online; accessed 8-November-2016], 2010.

Fytterer, T., von Savigny, C., Mlynczak, M., and Sinnhuber, M.: Model results of OH airglow considering four different wavelength regions to derive night-time atomic oxygen and atomic hydrogen in the mesopause region, Atmospheric Chemistry and Physics, 19, 1835–1851, https://doi.org/10.5194/acp-19-1835-2019, https://www.atmos-chem-phys.net/19/1835/2019/, 2019.

Gao, H., Nee, J.-B., and Xu, J.: The emission of oxygen green line and density of O atom determined by using ISUAL and SABER measurements, Annales Geophysicae, 30, 695–701, https://doi.org/10.5194/angeo-30-695-2012, https://www.ann-geophys.net/30/695/2012/, 2012.

Gottwald, M., Diekmann, F.-J., and Diekmann, F.-J.: ENVISAT - SCIAMACHY's Host, in: SCIAMACHY - Exploring the Changing Earth's Atmosphere, XVI, 225, Springer Netherlands, https://doi.org/10.1007/978-90-481-9896-2, 2011.

Hays, P. B., Abreu, V. J., Dobbs, M. E., Gell, D. A., Grassl, H. J., and Skinner, W. R.: The high-resolution doppler imager on the Upper Atmosphere Research Satellite, Journal of Geophysical Research: Atmospheres, 98, 10 713–10 723, https://doi.org/10.1029/93JD00409, https://agupubs.onlinelibrary.wiley.com/doi/abs/10.1029/93JD00409, 1993.

Kalogerakis, K. S.: A previously unrecognized source of the O_2 Atmospheric band emission in Earth's nightglow, Science Advances, 5, https://doi.org/10.1126/sciadv.aau9255, http://advances.sciencemag.org/content/5/3/eaau9255, 2019.

Kalogerakis, K. S., Smith, G. P., and Copeland, R. A.: Collisional removal of OH(X2$\prod$, ν = 9) by O, O_2, O_3, N_2, and CO_2, Journal of Geophysical Research: Atmospheres, 116, https://doi.org/10.1029/2011JD015734, https://agupubs.onlinelibrary.wiley.com/doi/abs/10.1029/2011JD015734, 2011.

Kalogerakis, K. S., Matsiev, D., Sharma, R. D., and Wintersteiner, P. P.: Resolving the mesospheric nighttime 4.3 μm emission puzzle: Laboratory demonstration of new mechanism for OH(ν) relaxation, Geophysical Research Letters, 43, 8835–8843, https://doi.org/10.1002/2016GL069645, https://agupubs.onlinelibrary.wiley.com/doi/abs/10.1002/2016GL069645, 2016.

Kaufmann, M., Lehmann, C., Hoffmann, L., Funke, B., López-Puertas, M., Savigny, C., and Riese, M.: Chemical heating rates derived from SCIAMACHY vibrationally excited OH limb emission spectra, Advances in Space Research, 41, 1914 – 1920, https://doi.org/https://doi.org/10.1016/j.asr.2007.07.045, http://www.sciencedirect.com/science/article/pii/S0273117707008459, 2008.

Kaufmann, M., Ern, M., Lehmann, C., and Riese, M.: The response of atomic hydrogen to solar radiation changes, in: Climate And Weather of the Sun-Earth System (CAWSES): Highlights from a priority program, pp. 171–188, Springer Atmospheric Sciences, http://juser.fz-juelich.de/record/22385, 2013.

Kaufmann, M., Zhu, Y., Ern, M., and Riese, M.: Global distribution of atomic oxygen in the mesopause region as derived from SCIAMACHY O(^{1}S) green line measurements, Geophysical Research Letters, 41, 6274–6280, https://doi.org/10.1002/2014GL060574, https://agupubs.onlinelibrary.wiley.com/doi/abs/10.1002/2014GL060574, 2014.

Kyrölä, E., Tamminen, J., Sofieva, V., Bertaux, J. L., Hauchecorne, A., Dalaudier, F., Fussen, D., Vanhellemont, F., Fanton d'Andon, O., Barrot, G., Guirlet, M., Mangin, A., Blanot, L., Fehr, T., Saavedra de Miguel, L., and Fraisse, R.: Retrieval of atmospheric parameters from GOMOS data, Atmospheric Chemistry and Physics, 10, 11 881–11 903, https://doi.org/10.5194/acp-10-11881-2010, http://www.atmos-chem-phys.net/10/11881/2010/, 2010.

Kyrölä, E., Blanot, L., Tamminen, J., Sofieva, V., Bertaux, J. L., Hauchecorne, A., Dalaudier, F., Fussen, D., Vanhellemont, F., d'Andon, O. F., and Barrot, G.: Algorithm Theoretical Basis Document Version 3.0, Tech. Rep. GOM-FMI-TN-040, Finnish Meteorological Institute and ACRI-ST and LATMOS-IPSL and Institut d'Aéronomie Spatiale de Belgique, 2012.

Lacoursiére, J., Dyer, M. J., and Copeland, R. A.: Temperature dependence of the collisional energy transfer of OH(v=10) between 220 and 310 K, The Journal of Chemical Physics, 118, 1661–1666, https://doi.org/10.1063/1.1530581, https://doi.org/10.1063/1.1530581, 2003.

Lednyts'kyy, O., von Savigny, C., Eichmann, K.-U., and Mlynczak, M. G.: Atomic oxygen retrievals in the MLT region from SCIAMACHY nightglow limb measurements, Atmospheric Measurement Techniques, 8, 1021–1041, https://doi.org/10.5194/amt-8-1021-2015, https://www.atmos-meas-tech.net/8/1021/2015/, 2015.

Lednyts'kyy, O., von Savigny, C., and Weber, M.: Sensitivity of equatorial atomic oxygen in the MLT region to the 11-year and 27-day solar cycles, Journal of Atmospheric and Solar-Terrestrial Physics, 162, 136 – 150, https://doi.org/https://doi.org/10.1016/j.jastp.2016.11.003, http://www.sciencedirect.com/science/article/pii/S1364682616303911, layered Phenomena in the Mesopause Region, 2017.

Li, F., Liu, A. Z., and Swenson, G. R.: Characteristics of instabilities in the mesopause region over Maui, Hawaii, Journal of Geophysical Research: Atmospheres, 110, https://doi.org/10.1029/2004JD005097, https://agupubs.onlinelibrary.wiley.com/doi/abs/10.1029/2004JD005097, 2005.

Malhotra, G., Ruohoniemi, J. M., Baker, J. B. H., Hibbins, R. E., and McWilliams, K. A.: HF radar observations of a quasi-biennial oscillation in midlatitude mesospheric winds, Journal of Geophysical Research: Atmospheres, 121, 12,677–12,689, https://doi.org/10.1002/2016JD024935, https://agupubs.onlinelibrary.wiley.com/doi/abs/10.1002/2016JD024935, 2016.

Marsh, D. R., Garcia, R. R., Kinnison, D. E., Boville, B. A., Sassi, F., Solomon, S. C., and Matthes, K.: Modeling the whole atmosphere response to solar cycle changes in radiative and geomagnetic forcing, Journal of Geophysical Research: Atmospheres, 112, n/a–n/a, https://doi.org/10.1029/2006JD008306, http://dx.doi.org/10.1029/2006JD008306, d23306, 2007.

Massimo Cardaci, R. and Lannone, Q.: ENVISAT-1 Products Specifications - Volume 10:GOMOS Products Specifications, Tech. Rep. PO-RS-MDA-GS-2009/IDEAS-SER-IPF-SPE-1124, Serco SpA, 2012.

Mlynczak, M. G., Hunt, L. A., Marshall, B. T., Mertens, C. J., Russell, J. M., Siskind, D., Thompson, R. E., and Gordley, L. L.: Radiative constraints on the minimum atomic oxygen concentration in the mesopause region, Geophysical Research Letters, 40, 3777–3780, https://doi.org/10.1002/grl.50725, https://agupubs.onlinelibrary.wiley.com/doi/abs/10.1002/grl.50725, 2013a.

Mlynczak, M. G., Hunt, L. A., Mast, J. C., Thomas Marshall, B., Russell, J. M., Smith, A. K., Siskind, D. E., Yee, J.-H., Mertens, C. J., Javier Martin-Torres, F., Earl Thompson, R., Drob, D. P., and Gordley, L. L.: Atomic oxygen in the mesosphere and lower thermosphere derived from SABER: Algorithm theoretical basis and measurement uncertainty, Journal of Geophysical Research: Atmospheres, 118, 5724–5735, https://doi.org/10.1002/jgrd.50401, https://agupubs.onlinelibrary.wiley.com/doi/abs/10.1002/jgrd.50401, 2013b.

Mlynczak, M. G., Hunt, L. H., Mertens, C. J., Marshall, B. T., Russell, J. M., López Puertas, M., Smith, A. K., Siskind, D. E., Mast, J. C., Thompson, R. E., and Gordley, L. L.: Radiative and energetic constraints on the global annual mean atomic oxygen concentration in the mesopause region, Journal of Geophysical Research: Atmospheres, 118, 5796–5802, https://doi.org/10.1002/jgrd.50400, https://agupubs.onlinelibrary.wiley.com/doi/abs/10.1002/jgrd.50400, 2013c.

Mlynczak, M. G., Hunt, L. A., Russell, J. M., and Marshall, B. T.: Updated SABER Night Atomic Oxygen and Implications for SABER Ozone and Atomic Hydrogen, Geophysical Research Letters, 45, 5735–5741, https://doi.org/10.1029/2018GL077377, https://agupubs.onlinelibrary.wiley.com/doi/abs/10.1029/2018GL077377, 2018.

Offermann, D. and Grossmann, K. U.: Thermospheric density and composition as determined by a mass spectrometer with cryo ion source, Journal of Geophysical Research, 78, 8296–8304, https://doi.org/10.1029/JA078i034p08296, https://agupubs.onlinelibrary.wiley.com/doi/abs/10.1029/JA078i034p08296, 1973.

Offermann, D., Friedrich, V., Ross, P., and Zahn, U. V.: Neutral gas composition measurements between 80 and 120 km, Planetary and Space Science, 29, 747 – 764, https://doi.org/https://doi.org/10.1016/0032-0633(81)90046-5, http://www.sciencedirect.com/science/article/pii/0032063381900465, 1981.

Oliva, E., Origlia, L., Scuderi, S., Benatti, S., Carleo, I., Lapenna, E., Mucciarelli, A., Baffa, C., Biliotti, V., Carbonaro, L., Falcini, G., Giani, E., Iuzzolino, M., Massi, F., Sanna, N., Sozzi, M., Tozzi, A., Ghedina, A., Ghinassi, F., and Pedani, M.: Lines and continuum sky emission in the near infrared: Observational constraints from deep high spectral resolution spectra with GIANO-TNG, Astronomy & Astrophysics, 581, https://doi.org/10.1051/0004-6361/201526291, 2015.

Panka, P. A., Kutepov, A. A., Kalogerakis, K. S., Janches, D., Russell, J. M., Rezac, L., Feofilov, A. G., Mlynczak, M. G., and Yiğit, E.: Resolving the mesospheric nighttime 4.3 μm emission puzzle: comparison of the $CO_2(\nu_3)$ and $OH(\nu)$ emission models, Atmospheric Chemistry and Physics, 17, 9751–9760, https://doi.org/10.5194/acp-17-9751-2017, https://www.atmos-chem-phys.net/17/9751/2017/, 2017.

Panka, P. A., Kutepov, A. A., Rezac, L., Kalogerakis, K. S., Feofilov, A. G., Marsh, D., Janches, D., and Yiğit, E.: Atomic Oxygen Retrieved From the SABER 2.0- and 1.6-μm Radiances Using New First-Principles Nighttime OH(v) Model, Geophysical Research Letters, 45, 5798–5803, https://doi.org/10.1029/2018GL077677, https://agupubs.onlinelibrary.wiley.com/doi/abs/10.1029/2018GL077677, 2018.

Picone, J. M., Hedin, A. E., Drob, D. P., and Aikin, A. C.: NRLMSISE-00 empirical model of the atmosphere: Statistical comparisons and scientific issues, Journal of Geophysical Research: Space Physics, 107, SIA 15–1–SIA 15–16, https://doi.org/10.1029/2002JA009430, http://dx.doi.org/10.1029/2002JA009430, 1468, 2002.

Ratnam, M. V., Kumar, G. K., Murthy, B. V. K., Patra, A. K., Rao, V. V. M. J., Rao, S. V. B., Kumar, K. K., and Ramkumar, G.: Long-term variability of the low latitude mesospheric SAO and QBO and their relation with stratospheric QBO, Geophysical Research Letters, 35, https://doi.org/10.1029/2008GL035390, https://agupubs.onlinelibrary.wiley.com/doi/abs/10.1029/2008GL035390, 2008.

Riese, M., Offermann, D., and Brasseur, G.: Energy released by recombination of atomic oxygen and related species at mesopause heights, Journal of Geophysical Research: Atmospheres, 99, 14 585–14 593, https://doi.org/10.1029/94JD00356, https://agupubs.onlinelibrary.wiley.com/doi/abs/10.1029/94JD00356, 1994.

Rodgers, C. D.: Inverse methods for atmospheric sounding:theory and practice, World Scientific, 2000.

Russell, J. P. and Lowe, R. P.: Atomic oxygen profiles (80-94 km) derived from Wind Imaging Interferometer/Upper Atmospheric Research Satellite measurements of the hydroxyl airglow: 1. Validation of technique, Journal of Geophysical Research: Atmospheres, 108, 4662, https://doi.org/10.1029/2003JD003454, https://agupubs.onlinelibrary.wiley.com/doi/abs/10.1029/2003JD003454, 2003.

Russell, J. P., Ward, W. E., Lowe, R. P., Roble, R. G., Shepherd, G. G., and Solheim, B.: Atomic oxygen profiles (80 to 115 km) derived from Wind Imaging Interferometer/Upper Atmospheric Research Satellite measurements of the hydroxyl and greenline airglow: Local time-latitude dependence, Journal of Geophysical Research: Atmospheres, 110, https://doi.org/10.1029/2004JD005570, https://agupubs.onlinelibrary.wiley.com/doi/abs/10.1029/2004JD005570, 2005.

Sander, S., Abbatt, J., Barker, J., Burkholder, J., Friedl, R., Golden, D., Huie, R., Kurylo, M., Moortgat, G., Orkin, V., and Wine, P.: Chemical Kinetics and Photochemical Data for Use in Atmospheric Studies, Evaluation No. 17, 2011.

Schmidt, H., Brasseur, G. P., Charron, M., Manzini, E., Giorgetta, M. A., Diehl, T., Fomichev, V. I., Kinnison, D., Marsh, D., and Walters, S.: The HAMMONIA Chemistry Climate Model: Sensitivity of the Mesopause Region to the 11-Year Solar Cycle and CO_2 Doubling, Journal of Climate, 19, 3903–3931, https://doi.org/10.1175/JCLI3829.1, https://doi.org/10.1175/JCLI3829.1, 2006.

Sharma, R. D., Wintersteiner, P. P., and Kalogerakis, K. S.: A new mechanism for OH vibrational relaxation leading to enhanced CO_2 emissions in the nocturnal mesosphere, Geophysical Research Letters, 42, 4639–4647, https://doi.org/10.1002/2015GL063724, https://agupubs.onlinelibrary.wiley.com/doi/abs/10.1002/2015GL063724, 2015.

Sharp, W. E.: absolute concentrations of $O(^3P)$ in the lower thermosphere at night, Geophysical Research Letters, 7, 485–488, https://doi.org/10.1029/GL007i007p00485, https://agupubs.onlinelibrary.wiley.com/doi/abs/10.1029/GL007i007p00485, 1980.

Sharp, W. E.: The measurement of atomic oxygen in the mesosphere and lower thermosphere, Planetary and Space Science, 39, 617–626, 1991.

Sheese, P. E., McDade, I. C., Gattinger, R. L., and Llewellyn, E. J.: Atomic oxygen densities retrieved from Optical Spectrograph and Infrared Imaging System observations of O_2A-band airglow emission in the mesosphere and lower thermosphere, Journal of Geophysical Research: Atmospheres, 116, https://doi.org/10.1029/2010JD014640, https://agupubs.onlinelibrary.wiley.com/doi/abs/10.1029/2010JD014640, 2011.

Sheese, P. E., Llewellyn, E. J., Gattinger, R. L., and Strong, K.: OH Meinel band nightglow profiles from OSIRIS observations, Journal of Geophysical Research: Atmospheres, 119, 11,417–11,428, https://doi.org/10.1002/2014JD021617, https://agupubs.onlinelibrary.wiley.com/doi/abs/10.1002/2014JD021617, 2014.

Smith, A. K., Marsh, D. R., Mlynczak, M. G., and Mast, J. C.: Temporal variations of atomic oxygen in the upper mesosphere from SABER, Journal of Geophysical Research: Atmospheres, 115, https://doi.org/10.1029/2009JD013434, https://agupubs.onlinelibrary.wiley.com/doi/abs/10.1029/2009JD013434, 2010.

Smith, S. A., Fritts, D. C., and Vanzandt, T. E.: Evidence for a Saturated Spectrum of Atmospheric Gravity Waves, Journal of the Atmospheric Sciences, 44, 1404–1410, https://doi.org/10.1175/1520-0469(1987)044<1404:EFASSO>2.0.CO;2, https://doi.org/10.1175/1520-0469(1987)044<1404:EFASSO>2.0.CO;2, 1987.

Swenson, G., Yee, Y., Vargas, F., and Liu, A.: Vertical diffusion transport of atomic oxygen in the mesopause region consistent with chemical losses and continuity: Global mean and inter-annual variability, Journal of Atmospheric and Solar-Terrestrial Physics, 178, 47 – 57, https://doi.org/https://doi.org/10.1016/j.jastp.2018.05.014, http://www.sciencedirect.com/science/article/pii/S1364682617305552, 2018.

Tapping, K. F.: The 10.7cm solar radio flux (F10.7), Space Weather, 11, 394–406, https://doi.org/10.1002/swe.20064, https://agupubs.onlinelibrary.wiley.com/doi/abs/10.1002/swe.20064, 2013.

Thomas, R. J.: Atomic hydrogen and atomic oxygen density in the mesopause region: Global and seasonal variations deduced from Solar Mesosphere Explorer near-infrared emissions, Journal of Geophysical Research: Atmospheres, 95, 16 457–16 476, https://doi.org/10.1029/JD095iD10p16457, http://dx.doi.org/10.1029/JD095iD10p16457, 1990.

Tikhonov, A. and Arsenin, V.: Solutions of ill-posed problems, Scripta series in mathematics, Winston, https://books.google.de/books?id=ECrvAAAAMAAJ, 1977.

Trinks, H., Offermann, D., von Zahn, U., and Steinhauer, C.: Neutral composition measurements between 90- and 220-km altitude by rocket-borne mass spectrometer, Journal of Geophysical Research, 83, 2169–2176, https://doi.org/10.1029/JA083iA05p02169, 1978.

van Gijsel, J. A. E., Swart, D. P. J., Baray, J.-L., Bencherif, H., Claude, H., Fehr, T., Godin-Beekmann, S., Hansen, G. H., Keckhut, P., Leblanc, T., McDermid, I. S., Meijer, Y. J., Nakane, H., Quel, E. J., Stebel, K., Steinbrecht, W., Strawbridge, K. B., Tatarov, B. I., and Wolfram, E. A.: GOMOS ozone profile validation using ground-based and balloon sonde measurements, Atmospheric Chemistry and Physics, 10, 10 473–10 488, https://doi.org/10.5194/acp-10-10473-2010, http://www.atmos-chem-phys.net/10/10473/2010/, 2010.

Zhu, Y. and Kaufmann, M.: Atomic Oxygen Abundance Retrieved From SCIAMACHY Hydroxyl Nightglow Measurements, Geophysical Research Letters, 45, 9314–9322, https://doi.org/10.1029/2018GL079259, https://agupubs.onlinelibrary.wiley.com/doi/abs/10.1029/2018GL079259, 2018.

Zhu, Y., Kaufmann, M., Ern, M., and Riese, M.: Nighttime atomic oxygen in the mesopause region retrieved from SCIAMACHY O(^{1}S) green line measurements and its response to solar cycle variation, Journal of Geophysical Research: Space Physics, 120, 9057–9073, https://doi.org/10.1002/2015JA021405, https://agupubs.onlinelibrary.wiley.com/doi/abs/10.1002/2015JA021405, 2015.